Angle-variant metamaterial with reconfigurable phase modulation

Ao Chen,[1,2] Zhiwei Yang,[1,2] Stephan Anderson,[2,3] and Xin Zhang[1,2,*]

[1] *Department of Mechanical Engineering, Boston University, Boston, Massachusetts 02215, USA*
[2] *Photonics Center, Boston University, Boston, Massachusetts 02215, USA*
[3] *Chobanian & Avedisian School of Medicine, Boston University, Boston, Massachusetts 02118, USA*

(Received 20 September 2023; revised 6 December 2023; accepted 21 December 2023; published 31 January 2024)

Acoustic metamaterials introduce unprecedented ways by which to modulate acoustic waves in amplitude, phase, or both. Reconfigurable acoustic metamaterials yield advantages when compared to conventional metamaterials due to their flexible geometry and feasibility in realizing versatile functions. Herein, a reconfigurable acoustic metamaterial based on the angle-variant unit cells is proposed and demonstrated. Two orientation states of the V-shaped unit cell are selected to maximize the phase-shift-modulation effect. Furthermore, a metamaterial consisting of 18 components is fabricated, each of which is composed of 18 V-shaped unit cells in different orientation states. The components of the metamaterial may be readily reconfigured to deliver various phase-shift profiles in order to achieve on-demand acoustic functions. In addition, this rotation mechanism can be predictably improved by integrating motors for dynamic real-time reconfiguration. In this study, a series of acoustic functions, including acoustic focusing, splitting, and diffusion, are numerically and experimentally demonstrated. Additionally, an acoustic blocker design is also proposed. The results we present herein demonstrate the promise of our design in wave control. This work extends the realm of reconfigurable acoustic metamaterials and provides an alternative path for multifunctional acoustic wave modulation.

DOI: 10.1103/PhysRevApplied.21.014062

I. INTRODUCTION

Wave manipulation has always been a fundamental branch of acoustic physics. One prime example of wave control comes from optical lenses, which are optical components designed to focus or diverge light by precisely shaping their geometry. Recently, the flourishing development of acoustic metamaterials has demonstrated extraordinary acoustic characteristics for a variety of applications, such as negative refraction [1,2], acoustic insulation [3–6], and cloaking [7–9], among others [10–14]. Acoustic metamaterials are artificial structures that can deliver unconventional effective wave properties that are substantially different from those of natural materials. Notable for their extraordinary possibilities in manipulating acoustic waves, acoustic metamaterials typically emerge in the forms of Helmholtz resonators [15–20], membranes [21–23], and space-coiling structures [12,24,25]. They show excellent potential in covering the 2π phase span of acoustic waves in a relatively high transmission amplitude. Furthermore, acoustic metamaterials offer an elegant way to steer acoustic wave fronts and realize various functionalities, including acoustic focusing [26–28], nonreciprocal transmission [16,29–31], and wave-front modulation [1,32–34], among others [15,35–38].

Although the advent of acoustic metamaterials extends the realm of acoustic wave modulation, acoustic metamaterials are hindered in practical applications due to their fixed geometry and monofunctionality. In other words, once an acoustic metamaterial has been fabricated, its desired function is fixed. Therefore, a reconfigurable acoustic metamaterial that can be tuned for multifunctional wave control is highly desirable. To date, various methods have been proposed to realize reconfigurable wave control, such as coding metasurfaces [17,18,39–41], nonreciprocal phase modulations [16,42,43], and origami-inspired metamaterials [44]. Some of the reported approaches have been demonstrated in the electromagnetic field or based on adjusting the cavity volume of Helmholtz resonators; more solutions to reconfigurable wave control in acoustics are still needed.

Herein, we propose an alternative approach to the design of reconfigurable acoustic metamaterials in order to realize multifunctional acoustic wave manipulation. Our reported design is promising and robust for realizing versatile wave-manipulation functions, including acoustic focusing, splitting, and diffusion, as well as an off state for blocking incident acoustic energy. Here, we numerically and experimentally demonstrate the realization of high transmission with the desired phase shift based on simple V-shaped unit cells. Then, by designing desired phase-shift profiles, we are able to steer the acoustic waves to realize multifunctional acoustic manipulations. In the appendixes, we

*xinz@bu.edu

illustrate the simulation setups that are used to extract the bandgap and transmission behavior of the proposed structure. Additionally, photographs of the experimental apparatus are provided. Finally, we explore further options, including more rotated angles and multifunctional effects at different frequencies.

II. RESULTS AND DISCUSSION

A. Fundamental principle

The conventional Snell's law, which describes the relationship between the properties of the material and wave bending, governs the angles of incidence and refraction at the boundary of two media. Consider a plane wave incident at the boundary with an angle θ_i. The incident and refractive angle and the refractive index of the refractive and incident medium are related in the form of

$$\sin\theta_i / \sin\theta_r = n_r / n_i, \tag{1}$$

where θ_r is the angle of refraction and n_i and n_r are the refractive indices of the incident and refractive medium, respectively. However, with the discovery of the generalized Snell's law [45,46], a phase gradient is introduced as a new factor, in the form of

$$[k_0 n_i \sin\theta_i dx + (\Phi + d\Phi)] = [k_0 n_r \sin\theta_r dx + \Phi], \tag{2}$$

where $k_0 = 2\pi/\lambda_0$, λ_0 is the acoustic wavelength in air, dx is the distance between two infinitesimally close points, and Φ and $d\Phi$ are the phase and its discontinuities at this distance. If the phase gradient along the boundary is a

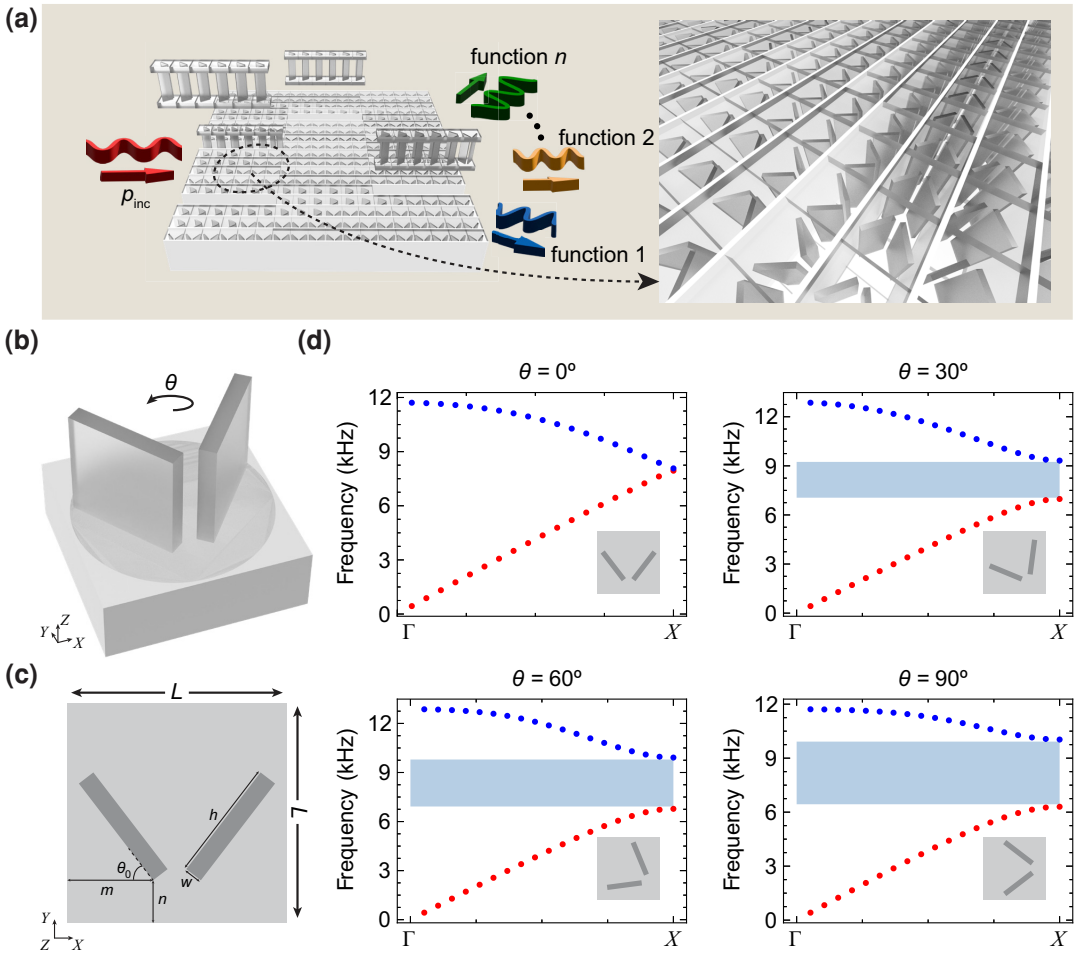

FIG. 1. (a) The concept of the V-shaped reconfigurable metamaterial for multifunctional wave control. (b) A schematic diagram of the V-shaped unit cells in a rotary mechanism. (c) The top view of the unit cells, with the following geometrical parameters: distance between the lowest point of the left arm to the left boundary $m = 7.18$ mm, distance between the lowest point of the left arm to the bottom boundary $n = 3.23$ mm, initial orientation of the left arm $\theta_0 = 37.5^\circ$, width of arm $w = 1.5$ mm, height of arm $h = 10.08$ mm, and length of the unit cells $L = 18$ mm. (d) The band structures of the unit cells as a function of different angular orientations $\theta = 0^\circ$, 30°, 60°, and 90°.

constant value, the equation is formatted into

$$\sin\theta_r n_r - \sin\theta_i n_i = \lambda_0 \nabla\Phi/2\pi, \tag{3}$$

where $\nabla\Phi = d\Phi/dx$ indicates the gradient of the phase discontinuity along the boundary. Thus, by designing and engineering a phase gradient along an interface, we can control the bending direction of the waves to deliver versatile functionalities. In the case of transmission through bulk materials, the incident plane wave has a sound pressure of $p_i = p_1 e^{-ikx}$, while the transmitted pressure would be $p_t = p_1 e^{-ikx+i\Phi}$, in which k represents the wave number and ϕ refers to the phase shift. For a specific bulk material, ϕ does not change as long as the thickness of the unit remains constant. In order to realize a reconfigurable phase gradient along the interface, a metamaterial consisting of an array of V-shaped unit cells is designed. By manipulating the angular orientation (initial state $\theta = 0°$) of each unit cell, the metamaterial can deliver multiple desired functions, as shown in Fig. 1(a). Figure 1(b) illustrates the V-shaped unit cell that we are proposing here, which consists of a base and two symmetric inclined arms. Its acoustic characteristics may be adjusted by rotating these two arms on the center point of the unit cell. The cross section of the unit cell and its geometrical parameters are illustrated in Fig. 1(c). We define three factors to describe the position of the left arm: m is the distance between the lowest point of the left arm to the left boundary, n is the distance between the lowest point of the left arm to the bottom boundary, and θ_0 is the initial orientation of the left arm. Meanwhile, the right arm is centrally symmetrical to the left arm. To ensure an optimal transmission behavior of the unit cell, the band structures of the unit cell at different angular orientations ($\theta = 0°$, 30°, 60°, 90°) are numerically obtained. In the case of aeroacoustic transmission, the mass density and the speed of sound in the air are set as $\rho_0 = 1.22$ kg/m^3, $c_0 = 343$ m/s. By solving the Floquet periodic conditions, the band structures of the unit cell at various frequencies are presented in Fig. 1(d). Intriguingly, the unit cell behaves inconsistently under different angular orientations. Given the reciprocity of acoustic wave propagation, rotation angles larger than 90° are not considered. When $\theta = 0°$, no band gap can be observed, indicating a high transmission along the ΓX direction at this frequency range. As we change the orientation of the unit cell, a partial band gap (blue domain) appears and becomes greater with a larger angle. The lower-frequency limits of the bandwidth are all larger than 6000 Hz, signifying that acoustic waves can transmit through the V-shaped unit cell ($\theta = 0°$, 30°, 60°, 90°) below 6000 Hz (see a detailed analysis of the bandgap and transmission behavior in the appendix). Therefore, we have chosen 6000 Hz as the operating frequency (corresponding to the wavelength of $\lambda \approx 57$ mm) in the following simulations and experiments to validate our proposed design.

B. Phase-array design

Similar to a V antenna providing phase shifts in an electric field [46], our proposed V-shaped unit cells are capable of generating phase shifts in acoustics. For maximum coverage of the phase shift, 18 metamaterial components are constructed, with each consisting of 18 V-shaped unit cells. As demonstrated in Fig. 2(a), every metamaterial component contains a different number of unit cells that rotate by either 90° (N) or 0° ($18 - N$). To optimize the reconfigurability while minimizing the testing errors, the metamaterial components are further divided into seven types of subcomponents, which contain N from 0 to 6, as shown in Fig. 2(b). Thus, each metamaterial component can be replaced with three subcomponents. By properly engineering the configuration of

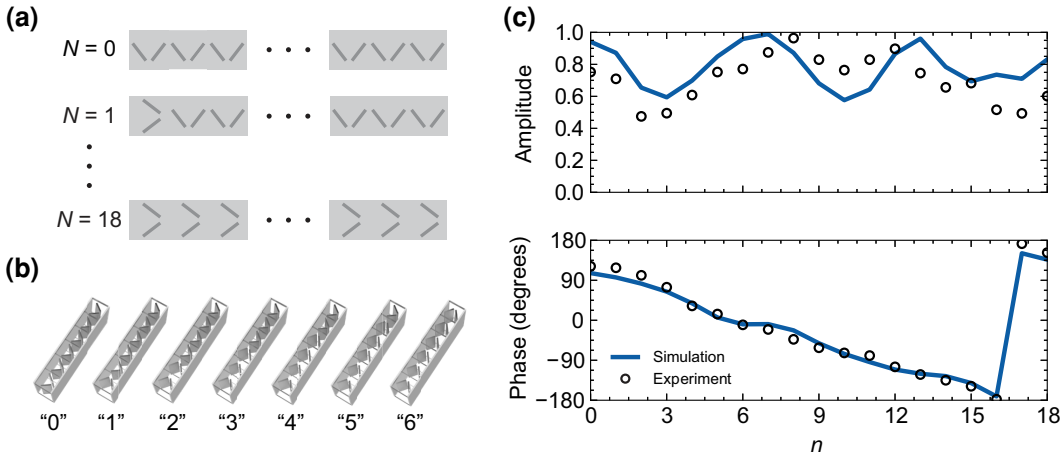

FIG. 2. (a) A schematic diagram of the metamaterial components composed of different numbers of $\theta = 90°$ rotated units (N). (b) A schematic diagram of seven types of subcomponents, labeled "0"–"6". (c) The simulated acoustic transmission of components and the comparison between the simulated and measured phase shifts that they provide.

subcomponents, the metamaterial can control its acoustic response and realize versatile wave control functions. Simulations are initially performed to characterize the transmission responses of the metamaterial components. The upper part of Fig. 2(c) shows the simulated transmission response of the metamaterial components as a function of different values of N for normally incident plane waves at 6000 Hz. Generally, components composed of different 90° unit cells maintain a transmission coefficient approximating 80%, consistent with a relatively high degree of acoustic energy transmission. Subsequently, the phase shifts of the transmitted waves are numerically and experimentally extracted, as shown in the bottom part of Fig. 2(c). By reconfiguring the building blocks of the metamaterial components, a phase shift covering almost a 2π range may be achieved. The black circles correspond to measured phase shifts of components when N varies from 0 to 18, suggesting a discrete phase shift in a 2π range with a step of 20°. It can be observed that the measured phase shifts agree well with the results obtained from numerical simulations. The agreement validates the conclusion that the metamaterial components can realize arbitrary phase modulation in a reconfigurable manner by mapping their subcomponents.

C. Versatile function designs

Given the metamaterial components demonstrate the feasibility of covering full-range phase shifts, a metamaterial is assembled into different configurations to achieve versatile functions. Simulations and experiments are both employed to validate the multifunctional characteristics of the metamaterial. Figure 3(a) is a schematic diagram of the experimental setup. For a given function, the metamaterial is redesigned into a specific configuration and placed into a two-dimensional waveguide. A sound source is placed in the front of the waveguide, generating plane waves incident on the metamaterial normally. A recording

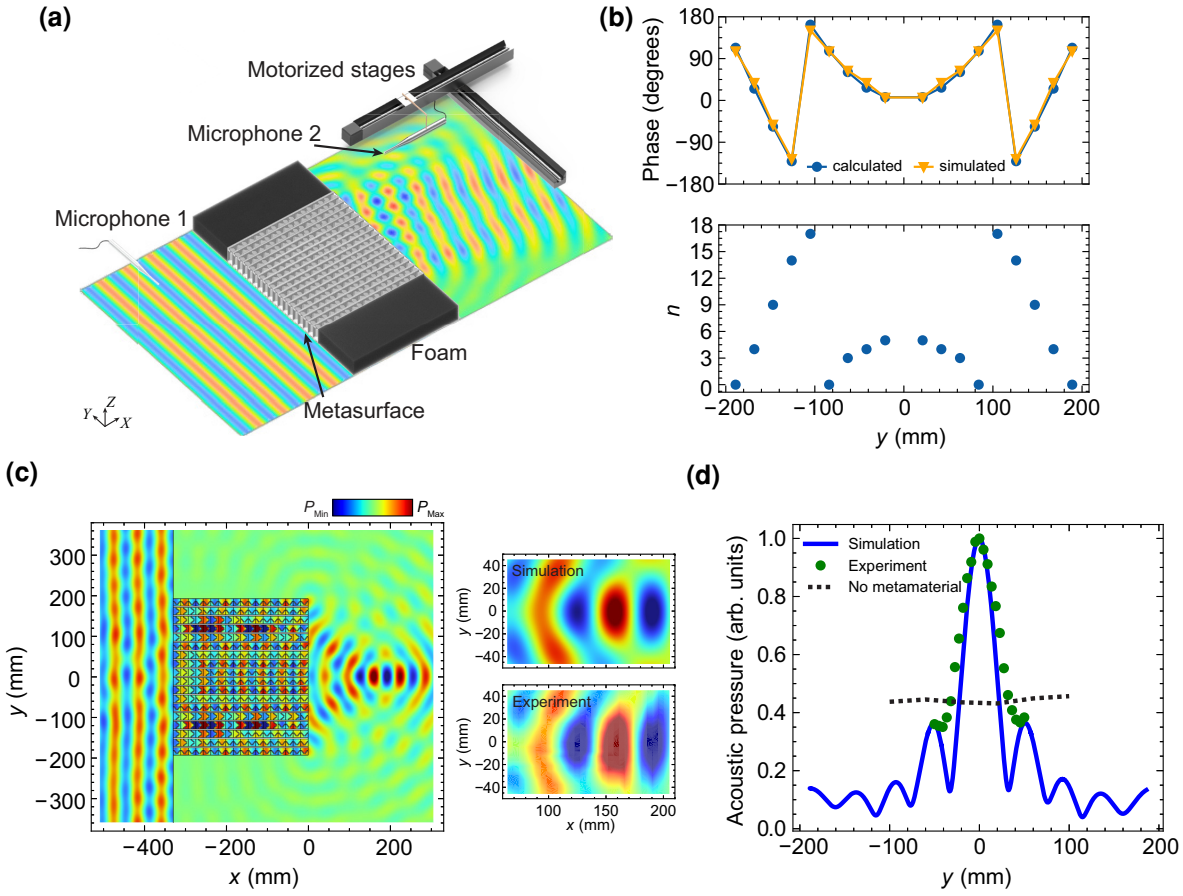

FIG. 3. (a) The schematic diagram of the experimental setup. (b) The calculated and simulated phase shifts that the metamaterial provides. The bottom figure represents the distribution of N along the y axis. (c) The simulated real component of the acoustic pressure field for acoustic focusing. The two inset figures correspond to the simulated (up) and measured (bottom) pressure field in the focal region. (d) The normalized magnitude of the acoustic pressure distribution along a cut line at $x = 0.2$ m. The blue line represents the simulated result, the green dots represent the measured result, and the black dashed line represents the measured acoustic pressure in the absence of the metamaterial.

microphone is placed behind the metamaterial to measure the transmitted acoustic pressure and by continuously changing its position, the pressure field of the desired area is acquired. Modulating the metamaterial to realize a given function requires initially calculating the required gradient phase shifts based on the generalized Snell's law, followed by arranging the subcomponents in the requisite configurations to achieve the desired function. Below, several functionalities are discussed and realized as a validation of our design.

1. Acoustic focusing

Acoustic focusing is of great interest to a variety of scenarios, including medical ultrasound imaging [35,47,48] and acoustic energy harvesting [49], among others [27,28]. Although acoustic focusing can be realized via conventional acoustic metamaterials, due to their fixed geometry and limited tunability in modulating phase shift, these metamaterials are unable to reshape the positions of the focal point once they are fabricated. Therefore, metamaterials that can be tailored to realize acoustic focusing at different locations are of interest. Compared to other tunable metamaterials that are typically based on Helmholtz resonators, the reconfigurable mechanism of this metamaterial is advantageous given the lack of a complex apparatus to precisely tune the cavity volume, as there are only two states that are available to the V-shaped unit cells, angular orientations of 0° and 90°. In order to focus the acoustic energy, the distribution of phase shifts along the metamaterial should follow

$$\varphi = k_0\left(\sqrt{(x-x_0)^2+(y-y_0)^2}-\sqrt{x_0^2+y_0^2}\right), \quad (4)$$

where (x_0, y_0) is the position of the focal point. In the case of acoustic waves being focused at (0.2 m, 0), the phase-shift distribution of the metamaterial along the y axis is calculated as the blue line with circle markers in Fig. 2(b). Taking advantage of the phase-shift-modulation ability of different types of subcomponents, the phase distribution may be mapped within different configurations of subcomponents. For example, when $y = 0.021$ m, the calculated phase shift is $\theta = 6.92°$ and, according to the measured data in Fig. 2(c), $N = 5$ fulfills the requisite criteria. Hence, three subcomponents are chosen ("0"×2 and "5"×1) and a simulated phase shift of 6.31° should be achieved. The mapping of the subcomponents is demonstrated by the blue dots in the bottom part of Fig. 3(b). As a comparison, the prediction of the phase shift is represented by the yellow line with triangle markers in the upper part of Fig. 3(b). The calculated and simulated results show

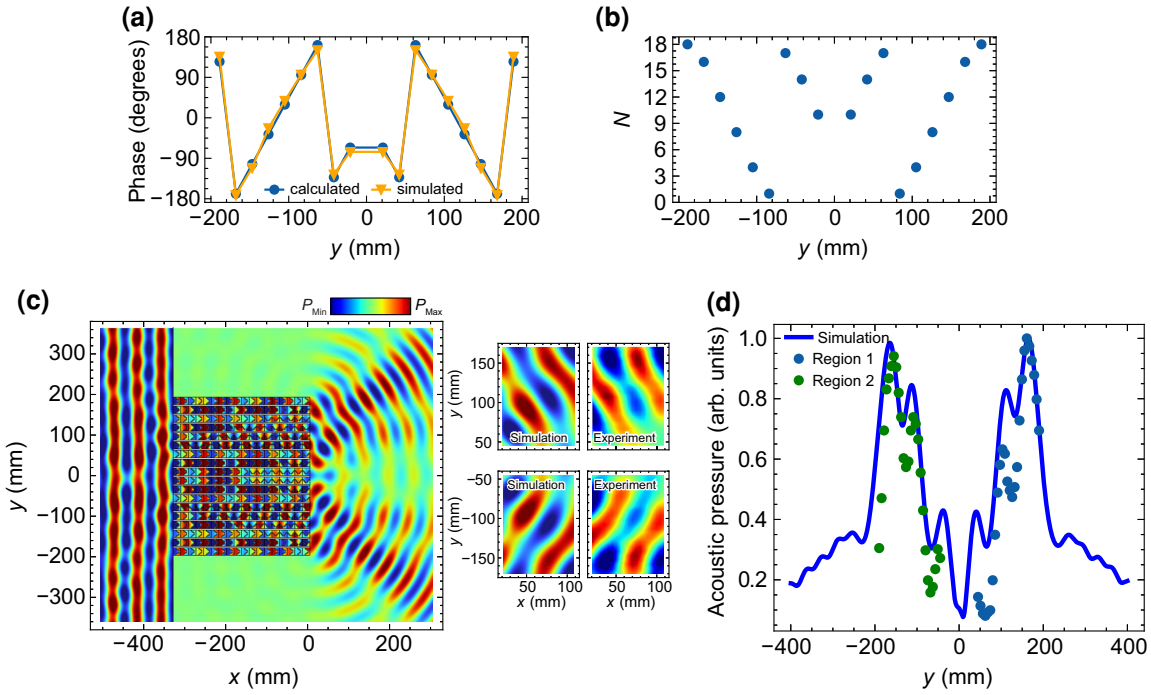

FIG. 4. (a) The calculated and simulated phase shifts that the metamaterial provides. (b) The distribution of N along the y axis. (c) The simulated real component of the acoustic pressure field for the acoustic wave-steering function. Two sets of inset figures correspond to simulated (left) and measured (right) pressure fields in the two wave-steering regions. (d) The normalized magnitude of the acoustic pressure distribution along a cut line at $x = 0.1$ m. The blue line represents the simulated result, the dark blue dots represent the measured result in region 1, and the green dots represent the measured pressure field in region 2. Here, region 1 refers to waves that are split "upward" and region 2 refers to waves that are split "downward" in the figure.

good agreement. Based on the acoustic focusing application, a simulation is undertaken, with the results shown in Fig. 3(c). For a plane wave incident from the left side, a focusing beam is present at the coordinate (0.2 m, 0). Additionally, the pressure distribution in the focusing region is measured and shown as the insets of Fig. 3(c). In order to quantify the resultant focusing, the acoustic pressure along a cut line ($x = 0.2$ m) is depicted in Fig. 3(d). The blue line and green dots correspond to the simulated and measured acoustic pressures normalized by their maximum pressure value along the cut line, respectively. The dashed black line represents the measured acoustic pressure in the absence of the metamaterial, normalized by the maximum pressure value in the presence of the metamaterial. It can be seen that, with the metamaterial, the pressure at the focal point ($y = 0$ m) is approximately 2.3 times larger than the pressure in the absence of the metamaterial. In the case of acoustic energy [squared acoustic pressure (p^2)] confinement, the presence of the metamaterial yields an approximately 5.3-fold enhancement. These results indicate that a robust focusing function is achieved.

2. Acoustic wave steering

As a second example, acoustic wave steering, a fundamental application of wave bending, is demonstrated. In the case of steering acoustic waves toward two directions symmetrically, the distribution of phase shift along the metamaterial should follow

$$\varphi = k_0 y \sin\theta_r, y \le 0; \quad \varphi = -k_0 y \sin\theta_r, y \ge 0. \tag{5}$$

Here, we select 30° as the refraction angle, following the same design procedure, and the phase-shift profile is presented by the blue line with circle markers in Fig. 4(a). The metamaterial is reconfigured and its subcomponents are mapped to match the calculated phase profile. The distribution of subcomponents for the acoustic wave-steering function is demonstrated in Fig. 4(b) and the prediction of the phase-shift profile it can deliver is shown by the yellow line with triangle markers in Fig. 4(a). Good agreement is achieved between the calculated and simulated phase-shift profiles. The corresponding simulated pressure field is illustrated in Fig. 4(c) and two splitting regions are further experimentally measured and compared with simulation results as the two groups of insets in Fig. 4(c). Finally, Fig. 4(d) shows the quantitative comparison between the simulated and measured normalized acoustic pressure at coordinate ($x = 0.1$ m), with the measured results agreeing well with results obtained from simulations.

3. Acoustic diffusion

Acoustic diffusers are used to transmit acoustic energy in all directions [15,40,50]. By diffusing acoustic energy evenly in space, diffusers are of interest in applications

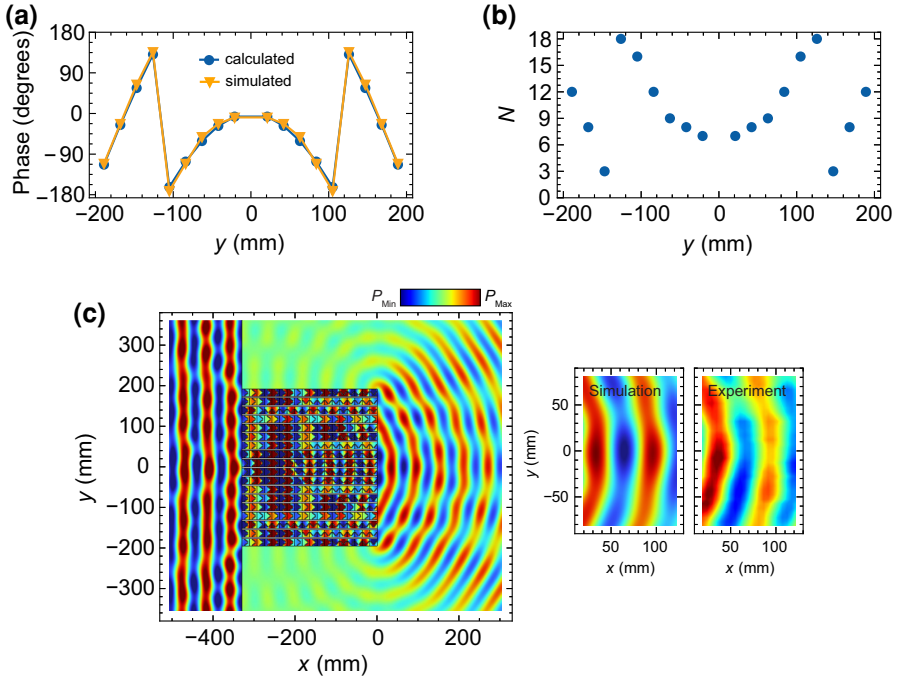

FIG. 5. (a) The calculated and simulated phase shifts that the metamaterial provides. (b) The distribution of N along the y axis. (c) The simulated real component of the acoustic pressure field for the acoustic diffusion function. The two inset figures correspond to the simulated (left) and measured (right) pressure field in the region of interest.

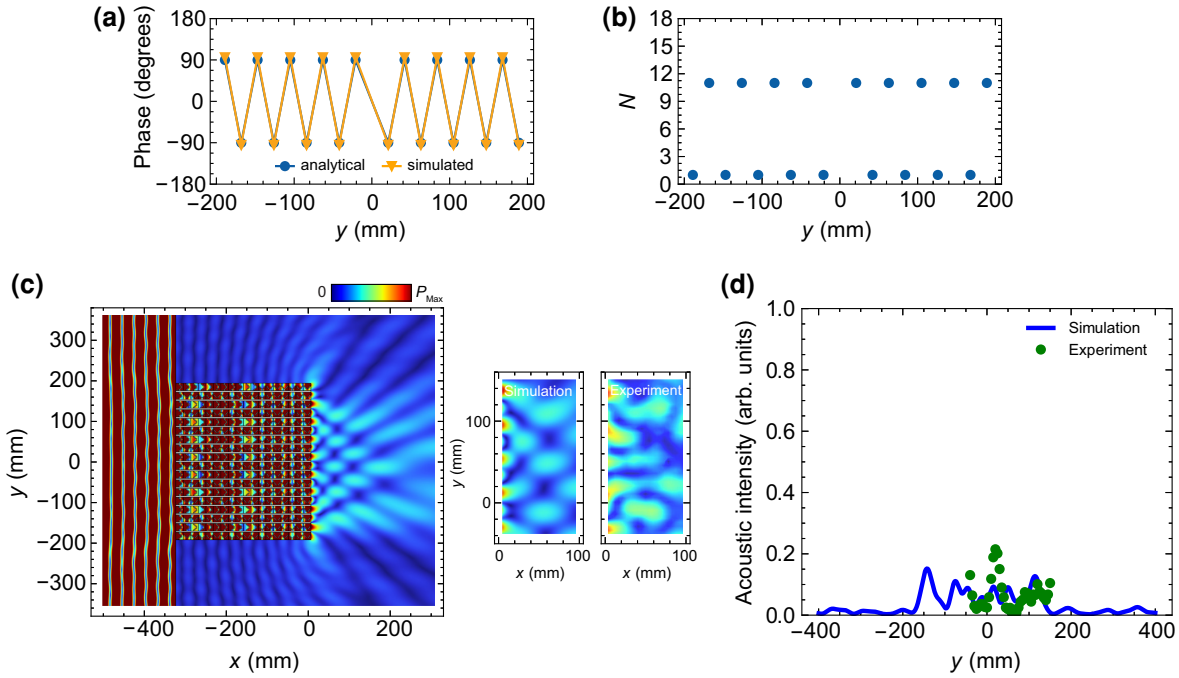

FIG. 6. (a) The calculated and simulated phase shifts that the metamaterial provides. (b) The distribution of N along the y axis. (c) The simulated magnitude of the acoustic pressure field for acoustic blocking. The two inset figures correspond to the simulated (left) and measured (right) pressure field in the acoustic transmitted region. Surface wave patterns can be observed close to the left boundary of the inset figures. (d) The normalized acoustic energy distribution along a cut line at $x = 0.08$ m. The blue line represents the simulated result, while the green dots represent the measured results.

such as noise control, ultrasound imaging, and other areas of architectural acoustics. Conventional Schroeder's diffusers are limited due to their bulk geometries and performance at mid- and high frequencies. By adjusting the configuration of the metamaterial, an acoustic diffuser operating at 6000 Hz is demonstrated herein. As the back propagation of acoustic focusing [16,51], the equation to calculate the phase profile of acoustic diffusion is the opposite of Eq. (4) and is expressed as

$$\varphi = k_0 \left(\sqrt{x_0^2 + y_0^2} - \sqrt{(x - x_0)^2 + (y - y_0)^2} \right). \quad (6)$$

Thus, the subcomponents of the metamaterial are mapped to match the desired phase profile, which is presented by the blue line with circle markers in Fig. 5(a). The distribution of subcomponents for the acoustic diffusion function is demonstrated in Fig. 5(b) and the prediction of the phase-shift profile is shown by the yellow line with triangle markers in Fig. 5(a). Simulation and experiments are subsequently undertaken and a satisfactory diffuse transmission effect can be observed in Fig. 5(c).

4. Off state

Lastly, in addition to multiple wave-manipulation functions, the feasibility of the metamaterial functioning as an acoustic blocker is also notable. This off-state function is achieved via the destructive interference resulting from the interaction between transmitted waves. The intensity of the interference is determined by the amplitude and phase of the propagating acoustic waves. To maximize the interference intensity, two metamaterial components ($N = 1$ and $N = 11$) are selected. The phase-shift difference between two adjacent components is close to π (96° and −94° and they share similar transmission amplitudes (of 0.79 and 0.74, respectively), which further advances the complete interference.

Therefore, by configuring components in a repetitive manner, blocking of the acoustic energy is achieved, resulting in a low transmittance. The analytical and simulated phase profiles for the off state are presented in Fig. 6(a) and the arrangement of the components is shown in Fig. 6(b). The simulated and measured absolute acoustic pressure field ($|P|$) are illustrated in Fig. 6(c). Notably, the surface wave along the y axis can be observed at the leftward boundary of the insets, indicating the strong interference between waves passing through adjacent components. In order to quantify the resultant acoustic blocking effect, the acoustic energy ($|P|^2$) along a cut line ($x = 0.08$ m) is depicted in Fig. 6(d). The blue line corresponds to the simulated acoustic energy normalized by the incident acoustic energy, while the green dots represent the measured acoustic energy that is normalized by the maximum acoustic energy at the same location in the absence of the

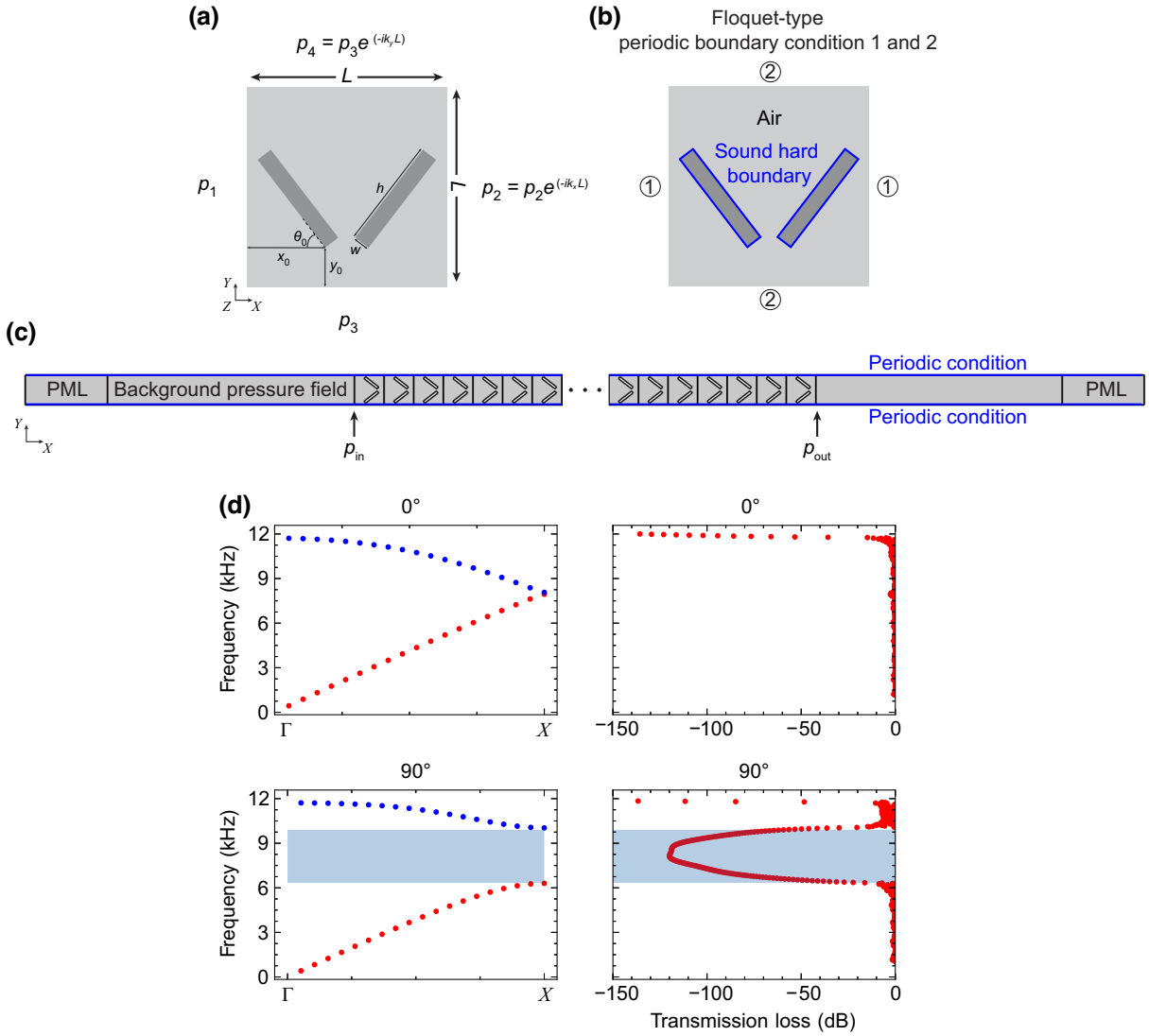

FIG. 7. (a) A schematic diagram of acoustic waves propagating through a unit cell. (b) The simulation setup for evaluating the band structure of the unit cell. (c) The simulation setup to derive the transmission loss of a finite array consisting of 18 unit cells. (d) A comparison between the band structures and transmission loss of 18 unit cells at different configurations (0° or 90° state).

metamaterial. The simulated and measured results show good consistency in the measured region, suggesting an acoustic energy transmission generally lower than 10%.

III. CONCLUSIONS

In this study, we have designed and demonstrated an acoustic metamaterial that can be reconfigured to deliver versatile wave-control functions. The proposed acoustic metamaterial is composed of V-shaped unit cells, which offer varied acoustic characteristics by rotating their arms to different orientations. Through the composition of unit cells into various configurations, full coverage of a 2π phase shift is realized. Based on this phase modulation methodology and by following the generalized Snell's law, we have numerically and experimentally shown the full capability of the metamaterial to steer acoustic waves, including acoustic focusing, splitting, and diffusion. Moreover, by leveraging destructive interference by mapping the metamaterial in a specific repetitive manner, we have been able to switch off the functionality of the metamaterial to achieve a low acoustic energy transmission. Compared to previous studies of metamaterials, which are typically fixed in functionality once they are fabricated, the proposed metamaterial yields a tunability capable of delivering multiple functions. Additionally, our metamaterial does not need costly or time-consuming fabrication, with only seven distinct types of subcomponents being required to deliver the desired functions. The discrete phase shifts enabled by our design ensure continuous and accurate modulation of incident acoustic waves. Moreover, if this rotation methodology can be combined with

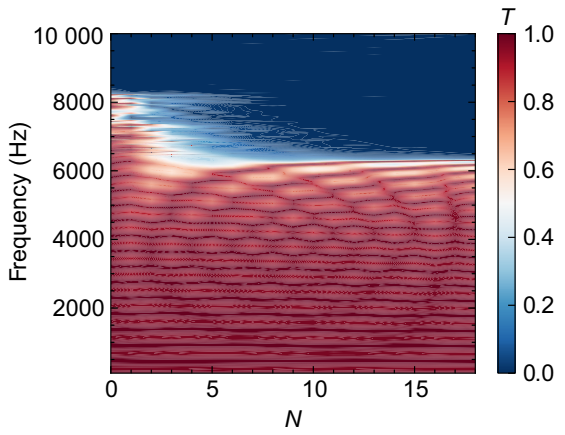

FIG. 8. The transmission coefficient of the unit-cell array composed of different numbers of $\theta = 90^{\circ}$ rotated units ($N = 0$–18) in the frequency range from 0 to 10 000 Hz.

an external apparatus such as a motor, a dynamic real-time phase modulation can be achieved. This study extends the realm of reconfigurable acoustic metamaterials and takes a step forward toward versatile acoustic wave manipulation. With further refinements, our design may be improved toward dynamic on-demand reconfiguration, broadband operation frequencies, and optimization of the orientation angles to achieve more reliable multifunction wave control. The reported metamaterial offers a pathway toward realizing reconfigurable acoustic technologies, applicable to a myriad of acoustic applications.

ACKNOWLEDGMENTS

The authors would like to thank Boston University Photonics Center for funding and technical support.

APPENDIX A: NUMERICAL SIMULATIONS

The numerical simulations were performed using the COMSOL MULTIPHYSICS 6.0 finite-element software, via the "Pressure Acoustics, Frequency Domain" (ACPR) module. All models are two-dimensional models. In all simulations, the background medium is set as air ($\rho_0 = 1.22$ kg/m^3, $c_0 = 343$ m/s). The outer frames of solids are set as sound hard boundaries. The band structures in Fig. 1 are determined with the eigenfrequency study. Floquet periodic boundary conditions are applied to the sides of the unit cell. In Figs. 2–6, a frequency-domain study is deployed to determine the acoustic transmission, the phase shift, and the pressure fields. Plane waves are incident normally with an amplitude of 1 Pa. Perfectly matched layers (PML) are adopted to reduce unwanted reflections at surrounding boundaries.

APPENDIX B: EXPERIMENTAL MEASUREMENTS

The metamaterial subcomponents were fabricated by a commercial stereolithography-based three-dimensional printer (Form 3+). The metamaterials were assembled with fabricated subcomponents and placed in a planar waveguide. The top and bottom sides of the waveguide were placed with acrylic boards, while the sides of the waveguide were filled with absorbing foam to reduce unnecessary acoustic reflection at the boundaries. A loudspeaker with a side length of 10 cm was used as the point source and placed 60 cm (approximately 10.5λ) from the metamaterial to generate plane waves. The transmitted acoustic pressure field was acquired with two microphones (Brüel & Kjær Type 4138 microphone), with one fixed close to the loudspeaker to record as a reference signal

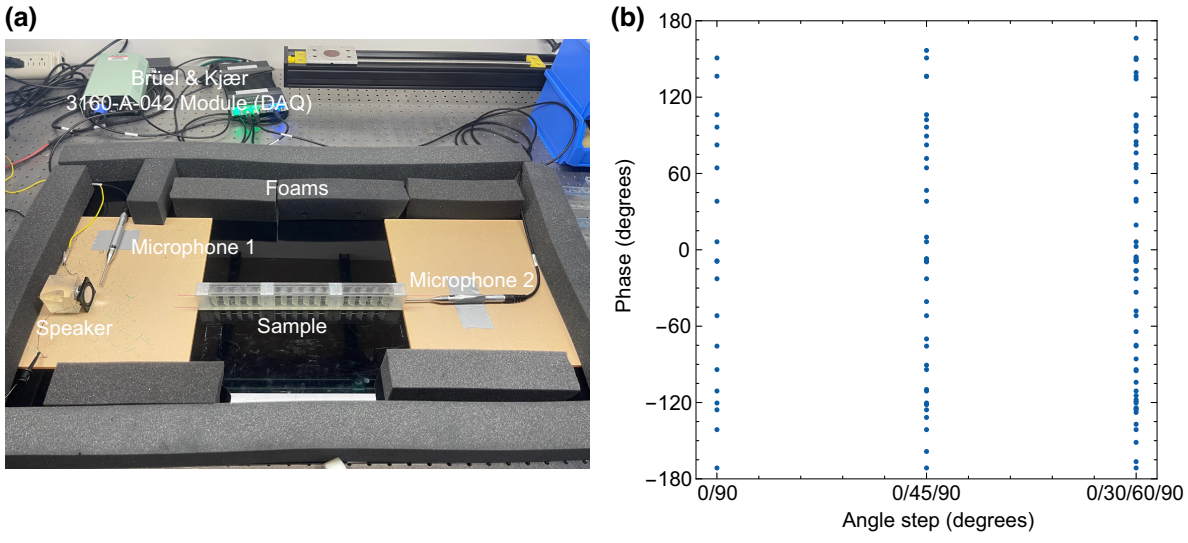

FIG. 9. (a) The experimental setup to measure the phase shift. (b) Phase-shift optimization by bringing in more orientation states of unit cells.

while the other was attached to a two-dimensional motorized linear stage (VELMEX BiSlide) on the transmission side. Point-to-point scanning was performed with a step of 0.5 cm in the area of interest. The measured data were recorded and analyzed by the Brüel & Kjær 3160-A-042 module.

APPENDIX C: BAND STRUCTURES AND TRANSMISSION BEHAVIOR

We can numerically derive the band structures of the unit cell using the Floquet-type periodic boundary condition in COMSOL MULTIPHYSICS. Ignoring the time term, the pressure field at different boundaries of the unit cell can be represented as p_1, $p_2 = p_1 e^{-ik_x L}$, p_3, and $p_4 = p_3 e^{-ik_y L}$, as shown in Fig. 7(a). Here, k_x and k_y represent wave vectors oriented along the x and y directions, respectively. The simulation setup used to derive the band structures of the unit cell is illustrated in Fig. 7(b). Given the high impedance mismatch between the solid frames and air, the frames of two arms are set as sound hard boundaries. Two sets of Floquet-type periodic boundary conditions are applied at the side boundaries of the unit cell. Subsequently, a simulation is performed to calculate the transmission loss of a finite array using the setup depicted in Fig. 7(c). Perfect-matched layers (PMLs) are applied at both ends of the geometry to minimize unwanted acoustic reflections. A background pressure field is applied in the front part of the waveguide, with an incident acoustic pressure of 1 Pa toward the positive x direction. To analyze the propagation behavior of unit cells, a finite array composed of 18 unit cells is placed at the center of the waveguide, while the top and bottom boundaries are set as periodic boundary conditions. The band structures of the unit cell are then examined at orientations of 0° and 90°, as depicted in the first column of Fig. 7(d), while the transmission loss of a finite array consisting of 18 unit cells is analyzed at the corresponding configurations shown in the second column.

Figure 8 illustrates the effect of numbers of $\theta = 90°$ rotated units (N) on acoustic transmission at different frequencies. Within a finite array of 18 unit cells, it can be observed that the transmission of acoustic energy is maintained at a relatively high amplitude below 6000 Hz, which agrees well with the band-structure analysis in Fig. 7(d). This result demonstrates that the proposed structures are capable of achieving broadband phase modulation.

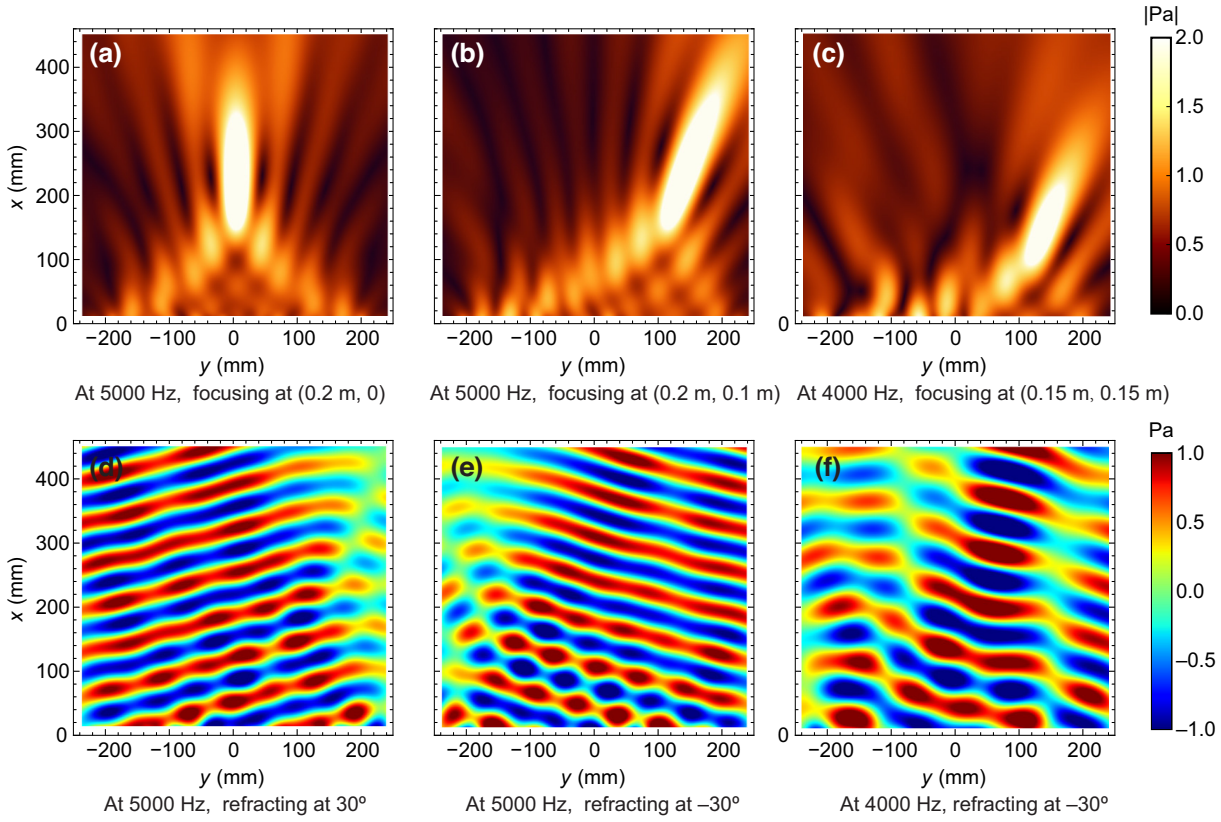

FIG. 10. Simulated results of acoustic wave steering at different frequencies.

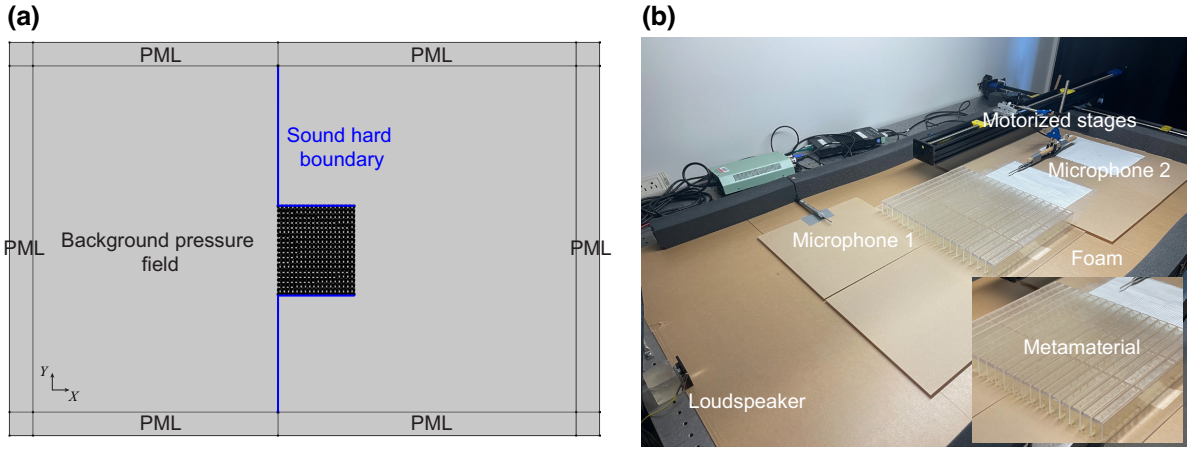

FIG. 11. (a) The simulation setup to derive the acoustic pressure field on the transmitted side. (b) The experimental setup to measure the pressure field.

APPENDIX D: THE EXPERIMENTAL SETUP TO MEASURE PHASE-SHIFT AND ROTATION-ANGLE OPTIMIZATION

Figure 9(a) shows the experimental setup to measure the phase shift of a finite array (the top layer of the waveguide is not shown). Foam is placed along the sides to reduce unwanted reflection. Two microphones are placed to record the acoustic pressure before and after the sample. The signal generation and data collection are all controlled by the Brüel & Kjær 3160-A-042 Module.

In the main text, we have selected two states of the unit cells, which are $\theta = 0°$ and $90°$, to achieve a discrete phase shift in a 2π range with a step of $20°$. To optimize for a more detailed phase-modulation effect, more adjustable states of unit cells are required. Figure 9(b) shows three sets of simulated phase-modulation effects of a finite array consisting of 18 unit cells. When the available states of each unit cell increase from two states ($\theta = 0°$ and $90°$) to three ($\theta = 0°, 45°$, and $90°$) and four states ($\theta = 0°, 30°, 60°$ and $90°$), the achieved phase shift covers a larger area.

APPENDIX E: DEMONSTRATION OF MULTIFUNCTIONALITIES OPERATING AT DIFFERENT FREQUENCIES

As shown in Fig. 8, the proposed metasurface has the potential to maintain a high transmission coefficient below 6000 Hz. Here, Figs. 10(a) and 10(b) demonstrate the reconfigurability of the proposed metasurface to tune the focal distance and the beam direction and then the same configuration as shown in Fig. 10(b) is operated at a different frequency of 4000 Hz. The result is shown in Fig. 10(c). Notably, the focal point in Fig. 10(c) shifts to a lower position due to different phase-modulation behaviors of the metasurface at different frequencies. Nevertheless, a solid acoustic focusing effect is still delivered. Similarly, the second row of Fig. 10 illustrates the functionalities of the proposed metasurface to tune the refraction angles of acoustic waves [Fig. 10(d), refracting at 30°; Fig. 10(e): refracting at $-30°$]. A metasurface in the same configuration is simulated at 4000 Hz. The result is shown in Fig. 10(f): a refraction angle of $-30°$ can still be observed but with a higher dispersion effect.

APPENDIX F: ACOUSTIC PRESSURE FIELD SIMULATION AND EXPERIMENTAL SETUP

Figure 11(a) shows the simulation setup. PMLs are applied to the surrounding regions to absorb the reflected and transmitted acoustic waves. A background pressure field is applied in the front part of the waveguide, with incident acoustic pressure 1 Pa toward the positive x-axis direction. In order to reduce the impact of a background pressure field on the transmission side, sound hard boundaries are applied on the blue lines. Figure 11(b) is a photograph of the experimental setup. Foam is used to absorb acoustic energy. A loudspeaker is placed in the far field to generate plane waves. Two microphones are used to record the acoustic pressure, with one placed on the loudspeaker side and the other attached to a motorized stage.

[1] Y. Xie, W. Wang, H. Chen, A. Konneker, B.-I. Popa, and S. A. Cummer, Wavefront modulation and subwavelength diffractive acoustics with an acoustic metasurface, Nat. Commun. **5**, 5553 (2014).

[2] Y. Xie, B.-I. Popa, L. Zigoneanu, and S. A. Cummer, Measurement of a broadband negative index with space-coiling

acoustic metamaterials, Phys. Rev. Lett. **110**, 175501 (2013).
[3] R. Ghaffarivardavagh, J. Nikolajczyk, S. Anderson, and X. Zhang, Ultra-open acoustic metamaterial silencer based on Fano-like interference, Phys. Rev. B **99**, 024302 (2019).
[4] A. Chen, X. Zhao, Z. Yang, S. Anderson, and X. Zhang, Broadband labyrinthine acoustic insulator, Phys. Rev. Appl. **18**, 064057 (2022).
[5] A. Chen, Z. Yang, X. Zhao, S. Anderson, and X. Zhang, Composite acoustic metamaterial for broadband low-frequency acoustic attenuation, Phys. Rev. Appl. **20**, 014011 (2023).
[6] C. Liu, J. Shi, W. Zhao, X. Zhou, C. Ma, R. Peng, M. Wang, Z. H. Hang, X. Liu, J. Christensen, *et al.*, Three-dimensional soundproof acoustic metacage, Phys. Rev. Lett. **127**, 084301 (2021).
[7] S. A. Cummer, B.-I. Popa, D. Schurig, D. R. Smith, J. Pendry, M. Rahm, and A. Starr, Scattering theory derivation of a 3D acoustic cloaking shell, Phys. Rev. Lett. **100**, 024301 (2008).
[8] J. Li and J. B. Pendry, Hiding under the carpet: A new strategy for cloaking, Phys. Rev. Lett. **101**, 203901 (2008).
[9] B.-I. Popa, L. Zigoneanu, and S. A. Cummer, Experimental acoustic ground cloak in air, Phys. Rev. Lett. **106**, 253901 (2011).
[10] Y. Cheng, C. Zhou, B. Yuan, D. Wu, Q. Wei, and X. Liu, Ultra-sparse metasurface for high reflection of low-frequency sound based on artificial Mie resonances, Nat. Mater. **14**, 1013 (2015).
[11] J. Zhang, W. Rui, C. Ma, Y. Cheng, X. Liu, and J. Christensen, Remote whispering metamaterial for non-radiative transceiving of ultra-weak sound, Nat. Commun. **12**, 3670 (2021).
[12] R. Ghaffarivardavagh, J. Nikolajczyk, R. Glynn Holt, S. Anderson, and X. Zhang, Horn-like space-coiling metamaterials toward simultaneous phase and amplitude modulation, Nat. Commun. **9**, 1349 (2018).
[13] H. Zhang, W. Zhang, Y. Liao, X. Zhou, J. Li, G. Hu, and X. Zhang, Creation of acoustic vortex knots, Nat. Commun. **11**, 3956 (2020).
[14] S. Gao, Y. Li, C. Ma, Y. Cheng, and X. Liu, Emitting long-distance spiral airborne sound using low-profile planar acoustic antenna, Nat. Commun. **12**, 2006 (2021).
[15] Y. Zhu, X. Fan, B. Liang, J. Cheng, and Y. Jing, Ultrathin acoustic metasurface-based Schroeder diffuser, Phys. Rev. X **7**, 021034 (2017).
[16] Y. Zhu, L. Cao, A. Merkel, S.-W. Fan, B. Vincent, and B. Assouar, Janus acoustic metascreen with nonreciprocal and reconfigurable phase modulations, Nat. Commun. **12**, 7089 (2021).
[17] Z. Tian, C. Shen, J. Li, E. Reit, Y. Gu, H. Fu, S. A. Cummer, and T. J. Huang, Programmable acoustic metasurfaces, Adv. Funct. Mater. **29**, 1808489 (2019).
[18] B. Xie, K. Tang, H. Cheng, Z. Liu, S. Chen, and J. Tian, Coding acoustic metasurfaces, Adv. Mater. **29**, 1603507 (2017).
[19] W. K. Cao, C. Zhang, L. T. Wu, K. Q. Guo, J. C. Ke, T. J. Cui, and Q. Cheng, Tunable acoustic metasurface for three-dimensional wave manipulations, Phys. Rev. Appl. **15**, 024026 (2021).
[20] K. Wu, J.-J. Liu, Y.-j. Ding, W. Wang, B. Liang, and J.-C. Cheng, Metamaterial-based real-time communication with high information density by multipath twisting of acoustic wave, Nat. Commun. **13**, 5171 (2022).
[21] C. Shen, Y. Xie, N. Sui, W. Wang, S. A. Cummer, and Y. Jing, Broadband acoustic hyperbolic metamaterial, Phys. Rev. Lett. **115**, 254301 (2015).
[22] J. Mei, G. Ma, M. Yang, Z. Yang, W. Wen, and P. Sheng, Dark acoustic metamaterials as super absorbers for low-frequency sound, Nat. Commun. **3**, 756 (2012).
[23] G. Ma, M. Yang, S. Xiao, Z. Yang, and P. Sheng, Acoustic metasurface with hybrid resonances, Nat. Mater. **13**, 873 (2014).
[24] Y. Zhu, N. J. Gerard, X. Xia, G. C. Stevenson, L. Cao, S. Fan, C. M. Spadaccini, Y. Jing, and B. Assouar, Systematic design and experimental demonstration of transmission-type multiplexed acoustic metaholograms, Adv. Funct. Mater. **31**, 2101947 (2021).
[25] G. Memoli, M. Caleap, M. Asakawa, D. R. Sahoo, B. W. Drinkwater, and S. Subramanian, Metamaterial bricks and quantization of meta-surfaces, Nat. Commun. **8**, 14608 (2017).
[26] T.-C. Zhang, J.-H. Chen, J. Qian, Y. Ge, S.-Q. Yuan, H.-X. Sun, and X.-J. Liu, Observation of ultrabroadband acoustic focusing based on V-shaped meta-atoms, Adv. Mater. Technol. **5**, 1900956 (2020).
[27] X. Fan, Y. Zhu, Z. Su, N. Li, X. Huang, Y. Kang, C. Li, C. Weng, H. Zhang, B. Liang, *et al.*, Ultrabroadband and reconfigurable transmissive acoustic metascreen, Adv. Funct. Mater. **33**, 2300752 (2023).
[28] Z. Hu, Y. Yang, L. Xu, Y. Jing, and H. Chen, Airy-beam-enabled binary acoustic metasurfaces for underwater ultrasound-beam manipulation, Phys. Rev. Appl. **18**, 024070 (2022).
[29] Y. Ding, Y. Peng, Y. Zhu, X. Fan, J. Yang, B. Liang, X. Zhu, X. Wan, and J. Cheng, Experimental demonstration of acoustic Chern insulators, Phys. Rev. Lett. **122**, 014302 (2019).
[30] C. He, X. Ni, H. Ge, X.-C. Sun, Y.-B. Chen, M.-H. Lu, X.-P. Liu, and Y.-F. Chen, Acoustic topological insulator and robust one-way sound transport, Nat. Phys. **12**, 1124 (2016).
[31] R. Fleury, D. L. Sounas, C. F. Sieck, M. R. Haberman, and A. Alù, Sound isolation and giant linear nonreciprocity in a compact acoustic circulator, Science **343**, 516 (2014).
[32] X. Jiang, Y. Li, B. Liang, J.-c. Cheng, and L. Zhang, Convert acoustic resonances to orbital angular momentum, Phys. Rev. Lett. **117**, 034301 (2016).
[33] Y. Li, C. Shen, Y. Xie, J. Li, W. Wang, S. A. Cummer, and Y. Jing, Tunable asymmetric transmission via lossy acoustic metasurfaces, Phys. Rev. Lett. **119**, 035501 (2017).
[34] Y. K. Chiang, S. Oberst, A. Melnikov, L. Quan, S. Marburg, A. Alù, and D. A. Powell, Reconfigurable acoustic metagrating for high-efficiency anomalous reflection, Phys. Rev. Appl. **13**, 064067 (2020).
[35] J. Chen, J. Xiao, D. Lisevych, A. Shakouri, and Z. Fan, Deep-subwavelength control of acoustic waves in an ultra-compact metasurface lens, Nat. Commun. **9**, 4920 (2018).

[36] K. Melde, A. G. Mark, T. Qiu, and P. Fischer, Holograms for acoustics, Nature **537**, 518 (2016).
[37] Y. Zhu, J. Hu, X. Fan, J. Yang, B. Liang, X. Zhu, and J. Cheng, Fine manipulation of sound via lossy metamaterials with independent and arbitrary reflection amplitude and phase, Nat. Commun. **9**, 1632 (2018).
[38] J. Hwan Oh, I. Kyu Lee, P. Sik Ma, and Y. Young Kim, Active wave-guiding of piezoelectric phononic crystals, Appl. Phys. Lett. **99**, 083505 (2011).
[39] L. Zhang, X. Q. Chen, S. Liu, Q. Zhang, J. Zhao, J. Y. Dai, G. D. Bai, X. Wan, Q. Cheng, G. Castaldi, *et al.*, Space-time-coding digital metasurfaces, Nat. Commun. **9**, 4334 (2018).
[40] T. J. Cui, M. Q. Qi, X. Wan, J. Zhao, and Q. Cheng, Coding metamaterials, digital metamaterials and programmable metamaterials, Light Sci. Appl **3**, e218 (2014).
[41] J.-P. Xia, D. Jia, H.-X. Sun, S.-Q. Yuan, Y. Ge, Q.-R. Si, and X.-J. Liu, Programmable coding acoustic topological insulator, Adv. Mater. **30**, 1805002 (2018).
[42] B.-I. Popa and S. A. Cummer, Non-reciprocal and highly nonlinear active acoustic metamaterials, Nat. Commun. **5**, 3398 (2014).
[43] Y. Zhai, H.-S. Kwon, and B.-I. Popa, Active willis metamaterials for ultracompact nonreciprocal linear acoustic devices, Phys. Rev. B **99**, 220301 (2019).
[44] S. Babaee, J. T. Overvelde, E. R. Chen, V. Tournat, and K. Bertoldi, Reconfigurable origami-inspired acoustic waveguides, Sci. Adv. **2**, e1601019 (2016).
[45] N. Yu, P. Genevet, M. A. Kats, F. Aieta, J.-P. Tetienne, F. Capasso, and Z. Gaburro, Light propagation with phase discontinuities: generalized laws of reflection and refraction, Science **334**, 333 (2011).
[46] X. Ni, N. K. Emani, A. V. Kildishev, A. Boltasseva, and V. M. Shalaev, Broadband light bending with plasmonic nanoantennas, Science **335**, 427 (2012).
[47] E. Macé, G. Montaldo, I. Cohen, M. Baulac, M. Fink, and M. Tanter, Functional ultrasound imaging of the brain, Nat. Methods **8**, 662 (2011).
[48] S. Jiménez-Gambín, N. Jiménez, J. M. Benlloch, and F. Camarena, Holograms to focus arbitrary ultrasonic fields through the skull, Phys. Rev. Appl. **12**, 014016 (2019).
[49] S. Qi and B. Assouar, Acoustic energy harvesting based on multilateral metasurfaces, Appl. Phys. Lett. **111**, 243506 (2017).
[50] X. M. Yang, X. Y. Zhou, Q. Cheng, H. F. Ma, and T. J. Cui, Diffuse reflections by randomly gradient index metamaterials, Opt. Lett. **35**, 808 (2010).
[51] S.-W. Fan, S.-D. Zhao, A.-L. Chen, Y.-F. Wang, B. Assouar, and Y.-S. Wang, Tunable broadband reflective acoustic metasurface, Phys. Rev. Appl. **11**, 044038 (2019).